Insect Biochemistry and Molecular Biology 42 (2012) 583–595

Contents lists available at SciVerse ScienceDirect

Insect Biochemistry and Molecular Biology

journal homepage: www.elsevier.com/locate/ibmb

Molecular dynamics and free energy studies on the carboxypeptidases complexed with peptide/small molecular inhibitor: Mechanism for drug resistance

Hong Zhang [a], Yao Yao [a], Huibin Yang [b], Xia Wang [a], Zhuo Kang [b], Yan Li [c], Guohui Li [d], Yonghua Wang [a,*]

[a] Bioinformatics Center, College of Life Sciences, State Key Laboratory of Crop Stress Biology for Arid Areas, Northwest A&F University, Shaanxi 712100, China
[b] State Key Laboratory of the Discovery and Development of Novel Pesticide, Shenyang Research Institute of Chemical Industry Co., Ltd., Shenyang 110000, China
[c] School of Chemical Engineering, Dalian University of Technology, Dalian 116012, China
[d] Laboratory of Molecular Modeling and Design, Chinese Academy of Sciences, Dalian, Liaoning 116024, China

ARTICLE INFO

Article history:
Received 18 January 2012
Received in revised form
12 April 2012
Accepted 16 April 2012

Keywords:
Metallocarboxypeptidases
Drug resistance
Potato carboxypeptidase inhibitor
Molecular dynamics simulations
Binding free energy

ABSTRACT

As one potent plant protease inhibitor, potato carboxypeptidase inhibitor (PCI) can competitively inhibit insect digestive metallocarboxypeptidases (MCPs) through interfering with its digestive system that causes amino acid deficiencies and leading to serious developmental delay and mortality. However, this effective biological pest control is significantly impaired by the PCI-resistant insect MCPs. Therefore, deep understanding of the resistant mechanism of insect MCPs is particularly necessary for designing new durable pest control regimen and developing effective pesticides. In this study, the binding of PCI and small molecular inhibitor THI to insect PCI-sensitive/-resistant MCPs and human MCP was investigated by docking, molecular dynamics (MD) simulations and thermodynamic analysis. The structural analysis from MD simulations indicates that the PCI-resistant mechanism of CPBHz is mainly dominated by the Trp277A, which changes the conformation of β8-α9 loop and therefore narrow the access to the active site of CPBHz, prohibiting the entrance of the C termini tail of PCI. Additionally, the insertion of Gly247A weakens the stabilization of CPBHz and PCI through disrupting the hydrogen bond formation with its surrounding residues. Furthermore, the predicted binding free energies gives explanation of structure affinity relationship of PCI and THI with MCPs and suggest that the electrostatic energy is the main contribution term affecting the difference in binding affinities. Finally, the decomposition analysis of binding free energies infers that the key residues Glu72, Arg127, Ile247/Leu247 and Glu270 are critical for the binding of PCI/THI to MCPs.

1. Introduction

Metallocarboxypeptidases (MCPs) are physiologically important zinc-dependent exopeptidases that catalyze the hydrolysis of peptide bonds at the C-terminus of peptides and proteins (Vendrell et al., 2000). Digestive MCPs, as a main subfamily of MCPs, localize in the digestive tract and function mainly in breakdown the intake proteins. At present, two subtypes of digestive MCPs have been identified, i.e. CPA and CPB, which show a preference for hydrophobic and lysine or arginine basic C-terminal residues, respectively (Gomis-Rüth, 2008). To avoid deleterious effects of digestive MCPs at improper times or locations, these enzymes are biosynthesized as inactive zymogens termed procarboxypeptidases (PCPs). After activated by trypsin or trypsin-like enzymes, the pro domain, a 90–95-residue globular N-terminal polypeptide, is then segregated from the PCPs, leading to the release of the active catalytic moiety. Structurally, the catalytic domain is consisted of a central twisted eight-stranded β-sheet flanked by eight α-helices, displaying a globular α/β hydrolase fold (Fernández et al., 2010). At the active site of digestive MCPs, the catalytically active Zn^{2+} ion is penta-coordinated by His69 ND1, Glu72 OE1, Glu72 OE2, His196 ND1 and a water molecule, exhibiting beautiful tetrahedron architecture (David and William, 1989).

Normally, plant-eating insects can cause severe damage to plants, especially to the economical crops. Interestingly, to resist the insect attack, most plant species can express different protease inhibitors (PIs) to hinder the function of insect digestive enzymes (Lawrence and Koundal, 2002). Among numerous PIs, the potato carboxypeptidase inhibitor (PCI), a 39-residue globular protein, can inhibit MCPs with the binding constant (K_i) in a nanomolar level (Hass et al., 1979; Rees and Lipscomb, 1982). However, insects are so smart and they have evolved many ways to alleviate the detriment

* Corresponding author. Tel./fax: +86 029 87092262.
E-mail address: yh_wang@nwsuaf.edu.cn (Y. Wang).

0965-1748/$ – see front matter © 2012 Elsevier Ltd. All rights reserved.
doi:10.1016/j.ibmb.2012.04.005

of plant PIs, such as the development of PI-insensitive digestive MCPs, or up-regulation of expression of the digestive enzymes (Wu et al., 1997). Some lepidopteran insects (Bolter and Jongsma, 1997; Brito et al., 2001; Jongsma et al., 1995), such as *Helicoverpa zea*, a devastating pest of cotton and other important crop plants, adopts the former plot to survive in the presence of PIs (Broadway, 1995; Harsulkar et al., 1999).

The recently resolved crystal structure of CPBHz (CPB of *H. zea*) demonstrates that this enzyme is a 314-residues polypeptide chain and its structure is conserved among different species (Bayés et al., 2005). The conformational changes within the α7-β8, β8-α9 loops and the α7 helix caused by Gly247A and Trp277A confer a specific insensitivity of CPBHz to PCI (Bayés et al., 2005). Despite the structure has been resolved, the deep insights into PCI-insensitive mechanism of CPBHz are still elusive. Furthermore, the crystal structure is a stable conformation and does not provide information when the enzyme undergoes a rapid equilibrium within few conformations. Additionally, the crystals may differ significantly from the true structure in certain regions, as the experimental conditions are different from the real life circumstances (Lee et al., 2008). Thus, some questions are naturally raised concerning with the resistant mechanism of CPBHz to PCI, that is, 1) why and how the aforementioned key residues affect the conformational change dynamically? 2) How these conformational events impact the active site entrance that impairs the proper interaction with PCI in a dynamic process?

To elucidate these issues, some theoretical techniques, such as molecular dynamic (MD) simulation that serves as a link between structure and dynamics by providing detailed atomic motions as a function of time (Wang et al., 2011, 2010; Xu et al., 2011), has been applied in this work. In addition, the absolute binding free energy calculations and free energy decomposition analyses were also employed to investigate the resistance of CPBHz to PCI and the selectivity of PCI to CPAHa (CPA of *Helicoverpa armigera*) and CPBh (CPB of human). Firstly, the interactions between MCPs and PCI, and typical small molecular inhibitor THI (the abbreviation for 1-((6-methyl-2-oxo-1,2-dihydroquinolin-3-yl)-methyl)-3-(1-phenylethy)-1-(thiop-hen-2-ylmethyl) thiourea) (Fernández et al., 2009a, Fig. 1) were analyzed. Secondly, to deeply explore the insensitivity and selectivity of MCPs, the binding free energies were calculated by the Molecular Mechanics-Poisson-Boltzmann Surface Area (MM/PBSA) method (Kollman et al., 2000). Finally, the free energy decomposition based on the molecular mechanics-generalized-Born surface area (MM/GBSA) method (Gohlke et al., 2003) was further carried out to analyze the binding interfaces of MCP–PCI and MCP–THI complexes.

2. Materials and methods

2.1. Initial structures preparation

The starting crystal structures of CPBHz, CPAHa and CPBh were retrieved from the RCSB Brookhaven Protein Database (http://www.pdb.org/pdb/home/home.do) (PDB entry codes were 2C1C, 1JQG and 1KWM, respectively) and the pro domain of CPAHa and CPBh were removed for obtaining their active forms in this study. The MCP–PCI complexes, employed as references in the MCP–PCI docking procedure, were built through superimposing the structure of corresponding MCP onto the bovine CPA–PCI complex (PDB entry code: 4CPA) and the PCI was extracted and merged into each MCP by using software PyMOL (DeLano, 2010). Of note, the missed residues (N-terminal residue Glu1i and C-terminal residue Gly39i, i means inhibitor) of crystallized PCI were not added for the noninvolvement in the inhibitive interaction between MCP and PCI (Rees and Lipscomb, 1982). For molecular docking purpose, all hydrogen atoms were subsequently added to the unoccupied valence of heavy atoms at the neutral state (pH = 7.0) for PCI and MCPs by biopolymer module of SYBYL package (Tripos, Inc.). Protein–protein docking and molecular superposition software Hex 6.3 (http://www.csd.abdn.ac.uk/hex/) (Ritchie and Kemp, 2000), and Surflex docking module of SYBYL were used to search the best binding poses of PCI and THI binding to MCPs, respectively.

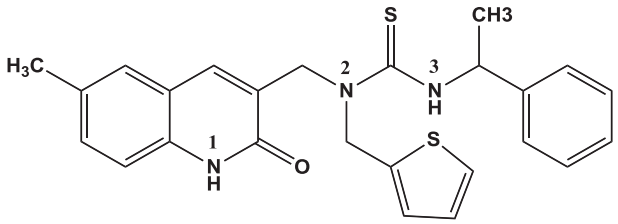

Fig. 1. Chemical structure of THI (1-((6-methyl-2-oxo-1,2-dihydroquinolin-3-yl)-methyl)-3-(1-phenylethy)-1-(thiophen-2-ylmethyl)thiourea).

2.1.1. MCP–PCI docking

Prior to docking, all water molecules of MCP crystal structures were removed. In order to guarantee the accuracy of the docking prediction, the corresponding MCP–PCI complex was adopted as a reference. Then the PCI was docked to the protein binding site by Hex "shape + electrostatics" based docking correlation with default parameters. Hex globally scanned the translational and rotational spaces of the molecules by surface complementarity and an electrostatic filter (Migliolo et al., 2010). From the 500 conformations presented by Hex, the best conformation with the lower energy was selected, which successfully reproduced the structure of the complex as judged by superimposing the docked results with the hypothetical crystal structure of the complex.

2.1.2. MCP–THI docking

Docking simulations were carried out using the Surflex, which combines Hammerhead's empirical scoring function with a molecular similarity method (morphological similarity) to generate putative poses of ligand fragments (Jain, 2003). As one of the most potent synthesized inhibitors against insect MCPs, THI was selected in our study. The small molecule THI downloaded from zinc database (http://zinc.docking.org/) was employed to perform the docking process. Two parameters, i.e., protomol-bloat and protomol-threshold, determine how far a potential ligand should extend outside of the concavity and how deep into the protein the atomic probes were used to define the protomol. For CPBHz, CPAHa and CPBh, the protomals were generated using the automatic approach without the crystal water molecules and the bloat and threshold were set to 0.50–0, 0.55–0 and 0.40–0, respectively. The docking approaches were validated by redocking of small molecules appearing in known crystal complex structures (L-phe-nyllactate/HFA for CPA (PDB code 2CTC) and an imidazole inhibitor/720 for CPB (PDB code 2JEW)), according to the strategy adopted in the literature (Fernández et al., 2009b). Before docking, the important ionizable residues (His69, Glu72, His196 and Glu270) were set at their default protonation states at the neutral state (pH = 7). The zinc ion was assigned a charge of +2.

Redocking is correct in terms of global conformation, orientation of the ligand and the root-mean-square deviation (RMSD) values (<1.6 Å for L-phenyllactate/HFA and <1.0 Å for the imidazole/720 in these docking processes, respectively), which also demonstrates the reliability of the docking protomol and parameters used.

2.2. Molecular dynamics (MD) simulations

Before MD simulations, a critical issue about the stability of zinc coordination environment should be mentioned. It is known that zinc ion directly involved in catalysis plays an important role in maintaining the physiological function of the MCPs, which may affect the protein-inhibitor interactions (Adler et al., 2005; Bayés et al., 2005; Estébanez-Perpiñá et al., 2001; Rees and Lipscomb, 1982). Up to now, three methods have been developed for tacking "missing parameter" problem regarding zinc ion of metalloprotein in MD simulations researches, namely nonbonded, semibonded and bonded models (Lin and Wang, 2010). Among them, the cationic pseudoatom representation (Pang, 2001), one of the semibonded models, was adopted with remarkable success in farnessyltransferase, beta-lactamase, phosphotriesterase and matrix metalloproteinase (Oelschlaeger et al., 2003; Pang, 1999, 2001; Pang et al., 2000). It solved the problem of maintaining the tetrahedral coordination of the metal throughout a molecular dynamic simulation without the loss of protein flexibility (Obiol-Pardo and Rubio-Martinez, 2006). Therefore, we employed this model to describe the zinc ion and its coordination environment for MCP–PCI and MCP–THI systems. In the cationic dummy atom model, the zinc ion was replaced by a neutral zinc atom centered at a tetrahedron formed by four massless dummy atoms with charge +0.5e, which were covalently connected to the zinc ion. The zinc ion was assigned only van der Waals parameters and interactions between the dummy atoms and amino acid residues were then computed using the conventional electrostatic interaction term. Here, the parameters were set referring to the strategy adopted in the literature (Lee et al., 2010). The +2e charge of the zinc ion was restored for the subsequent binding free energy analysis. Satisfyingly, the zinc ion coordination geometry obtained in this way was confirmed to be stable around 1.1 Å from the crystal structure throughout the MD simulations.

MD simulations were performed using the AMBER 10 package (Case et al., 2008) to get an equilibrated and reasonable structure. All of the initial structures were immersed in a rectangular box of TIP3P water extending at least 10 Å in each direction from the solute, and neutralized by adding sufficient Cl^- counter ions. The general atom force field (GAFF) (Wang et al., 2004) and the AMI-BCC (Jakalian et al., 2002) method were employed to set the ligand's parameters and charges. Standard AMBER force field for bioorganic systems (ff99SB) (Hummer et al., 2001) was chosen to depict the protein parameters.

Before the MD simulation, each system was gradually relaxed using 5000 steps of minimization procedure (2500 steepest descent steps and 2500 conjugate-gradient steps) to eliminate unfavorable contacts. Following this, MD simulations in the NPT ensemble with a target temperature of 300 K and a target pressure of 1 atm at a constant force of 2.0 kcal/mol $Å^{-2}$ constraining the protein atoms were performed. Subsequently, a 50 ps pressure-constant period to raise the density while still keeping the complex atoms constrained and a 500 ps equilibration were conducted. Finally, the production phase was run for 4 ns with a 2 fs time step under the periodic boundary conditions for each system. During the simulations process, the temperature was kept at 300 K by using Langevin dynamics with a collision frequency of 1 ps^{-1}. The long-range electrostatic interactions was treated by using the particle-mesh-Ewald (PME) method (Essmann et al., 1995), and all bonds involving the hydrogen atoms were constrained using SHAKE method (Ryckaert et al., 1977). During the sampling process, coordinates of each system were saved every 2 ps for analysis.

2.3. Binding free energy calculation

The 500 snapshots from the last 1 ns MD trajectories were collected to estimate the binding free energies. The MM/PBSA method, integrated in AMBER 10, was employed to predict the binding free energy. The MM/PBSA method is a versatile tool for calculating the binding free energies of a given protein–ligand complex or protein–protein/peptide complex, which incorporates the effects of thermal averaging with a force field/continuum solvent models to post-process a series of representative snapshots from MD trajectories (Hu et al., 2010). The binding free energies (ΔG_{bind}) were computed according to the following equations.

$$\Delta G_{bind} = \Delta H_{bind} - T\Delta S_{bind} \quad (1)$$

$$\Delta H_{bind} = \Delta E_{gas} + \Delta G_{sol} \quad (2)$$

$$\Delta E_{gas} = \Delta E_{int} + \Delta E_{vdw} + \Delta E_{ele} \quad (3)$$

$$\Delta G_{sol} = \Delta G_{PB} + \Delta G_{nP} \quad (4)$$

$$\Delta G_{nP} = \gamma(\mathrm{SASA}) + \beta \quad (5)$$

The sum of the molecular mechanical gas-phase energies (ΔE_{gas}), a standard force field energy, can be divided into internal energy (ΔE_{int}) as well as van der Waals (ΔE_{vdW}) and electrostatic energies (ΔE_{ele}) in Eq. (3). The solvation free energy (ΔG_{sol}) was calculated with a PB/SA model, which dissected solvation energy in two parts, that is, an electrostatic component (ΔG_{PB}) and a non-polar component (ΔG_{nP}). The electrostatic component was calculated using the PBSA program with the default cavity radii from the AMBER prmtop file. The dielectric constant was set to 1 for the interior solute and 80 for the surrounding solvent. The non-polar component was computed based on Eq. (5), where SASA was the solvent-accessible surface area estimated using the Molsurf program, which is part of the Amber 10 suite, with a solvent probe radius of 1.4 Å γ and β are empirical constants set to 0.0072 kcal mol^{-1} $Å^{-2}$ and 0.00 kcal mol^{-1}, respectively. Entropy contributions ($T\Delta S$) arising from changes in the translational, rotational and vibrational degrees of freedom were calculated using normal-mode analysis (Kottalam and Case, 1990) by the *nmode* program in AMBER 10. Since the normal-mode calculation of entropy is extremely time-consuming, only 20 snapshots for each system extracted from the last 1 ns were used to estimate the contribution of the entropy in our calculations. Before calculation, each snapshot was fully optimized for 10,000 steps using a distance-dependent dielectric of $4r_{ij}$ (r_{ij} is the distance between atoms i and j) until the root-mean-square deviation of the gradient vector was less than 0.0001 kcal mol^{-1} $Å^{-2}$.

2.4. Inhibitor–residue interaction decomposition

Due to the high computational demand and time-consuming of PB calculations, the interaction between each residue of protease and PCI as well as THI and each protease residue were computed using the MM/GBSA approach applied in the *MM/PBSA* module in AMBER 10. The binding free energy of each complex was decomposed per residue including three terms: van der Waals contribution (ΔG_{vdW}), electrostatic contribution (ΔG_{ele}) and solvation contribution ($\Delta G_{GB} + \Delta G_{SA}$).

$$\Delta G_{inhibitor-residue} = \Delta G_{vdW} + \Delta G_{ele} + \Delta G_{GB} + \Delta G_{SA} \quad (6)$$

where ΔG_{vdW} and ΔG_{ele} are non-bonded van der Waals interaction and electrostatic interactions between inhibitor and each MCP residue, which can be computed using the sander program in AMBER 10. The polar contribution (ΔG_{GB}) of solvation contribution ($\Delta G_{solvation}$) was computed using the generalized Born model, and the parameters for GB calculations were developed by Onufriev

et al. (2000). The charges used in GB calculations were taken from the AMBER parameter set. And the non-polar contribution of desolvation (ΔG_{SA}) was computed using the surface area. All energy components in Eq. (6) were calculated using the same snapshots as the free energy calculation.

3. Results and discussion

3.1. MCP–PCI complexes

3.1.1. Global structure behavior

To explore the dynamic stability of these three MCP–PCI complexes during the dynamics simulation, root-mean-square deviation (RMSD) values for the backbone atoms during the production phase relative to the starting structures along the entire MD trajectory were monitored, as plotted in Fig. 2.

The RMSD plots (Fig. 2B) indicate that the conformations of CPAHa–PCI and CPBh–PCI complexes achieve equilibrium at ~2.6 ns with the RMSD values around 1.5 Å, suggesting that these two conformations are stable. However, the RMSD of CPBHz–PCI complex increases gradually (from 1.3 to 3.3 Å) during the last 3 ns, which is due to the great oscillation of PCI tempestuous movement (Fig. 2A). This at least partly explains why the CPBHz prohibits the C-terminal tail (formed by Gly35i, Pro36i, Tyr37i and Val38i) of PCI to enter the active site (Bayés et al., 2005). In contrast to CPBHz, PCI closely binds to CPAHa and CPBh, as revealed by the low RMSD values.

The flexibility of the three systems is further analyzed by measuring the root-mean-square fluctuation (RMSF) of each residue from its time-average position, as displayed in Fig. 3. Generally, these three proteins share similar RMSF profiles (Fig. 3B). The average RMSFs for the CPBHz–PCI, CPAHa–PCI and CPBh–PCI complexes are 1.16 Å, 0.88 Å and 0.82 Å, respectively, which is consistent with previous RMSD results. The residues 212–216 (in the β6-α6 loop) in CPBHz fluctuate larger than those in the other proteins, while the residues 239–241 (in the α6-β7 loop) in CPAHa have larger fluctuations. And the terminal residues of MCPs are most flexible except the C-termini Tyr306 of CPBh hydrogen-bonded to Arg261, and the N-termini Ser1 of CPAHa that forms hydrogen bond (H-bond) with Glu20. As for the PCI in each system (Fig. 2A), we see that its N-terminal residues all have the greatest fluctuations, as they are freely exposed in solvent. Intriguingly, the C-terminal tail of PCI is very flexible in the CPBHz–PCI complex but stable in other two systems. This is due to the different binding modes of PCI to MCPs (see detailed discussions in section 3.1.3).

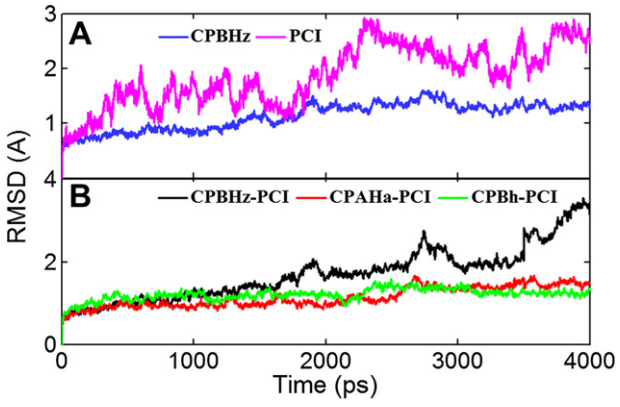

Fig. 2. A: Root-mean-square deviation (RMSD) of the backbone atoms (C, N, and C_α) of the PCI and CPBHz during the entire simulation course. B: RMSD of the backbone atoms (C, N, and C_α) of the CPBHz–PCI complex, the CPBHa–PCI complex and the CPBh–PCI complex with respect to the first snapshot as a function of time.

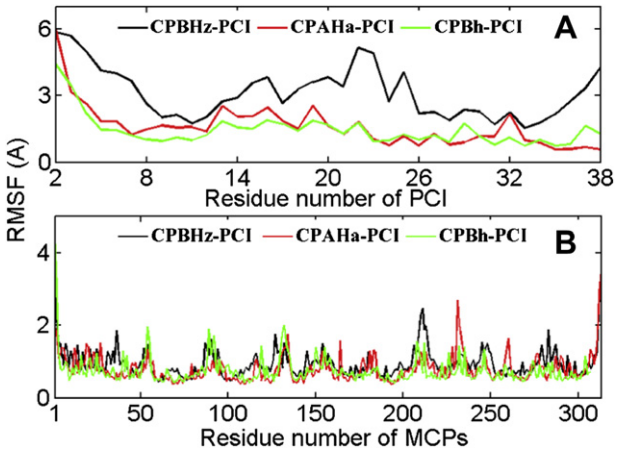

Fig. 3. A: Root-mean-square fluctuation (RMSF) of backbone atoms versus residue number of PCI in the three complexes over the entire simulated time. B: RMSF of backbone atoms versus residue number of the CPBHz, CPAHa and CPBh in each complex over the entire simulated time.

3.1.2. Binding free energy

To estimate the effect of conformational change resulted by Gly247A insertion and Trp277A substitution on binding free energies, the binding affinities were calculated and the results were listed in Table 1. Neglecting the entropic components, the relative binding free energy of CPAHa–PCI complex (−59.12 kcal/mol) is much more favorable than that of CPBh–PCI complex (−19.38 kcal/mol) and CPBHz–PCI complex (−16.33 kcal/mol), which is supported by a previous experiment (Bayés et al., 2005).

In order to get a better view on which energy has more impact on the binding affinities, the contributions from the electrostatic (ΔE_{ele}), van der Waals (ΔG_{vdw}), polar solvation (ΔG_{PB}) and non-polar solvation terms (ΔG_{np}) are further analyzed. The major favorable contributors are the electrostatic and van der Waals terms, whereas the polar solvation term opposes binding. And the non-polar solvation term, which corresponds to the burial of SASA, contributes slightly favorably. In details, the electrostatic contribution to CPAHa–PCI (−259.14 kcal/mol) is much greater than that to CPBHz–PCI (−73.41 kcal/mol) and CPBh–PCI (−57.64 kcal/mol). And the van der Waals contribution to CPBHz–PCI (−24.42 kcal/mol) is weaker than those to CPAHa–PCI (−56.04 kcal/mol) and CPBh–PCI (−64.89 kcal/mol). However, the net polar contributions ($\Delta E_{ele}+\Delta G_{PB}$) of the three complexes are unfavorable for the ligand binding (10.27, 4.66 and 53.07 kcal/mol for CPBHz–PCI, CPAHa–PCI and CPBh–PCI, respectively).

Table 1
Binding free energy estimates for MCP–PCI complexes.

Contribution	CPBHz–PCI		CPAHa–PCI		CPBh–PCI	
	Mean	Std	Mean	Std	Mean	Std
ΔE_{ele}	−73.41	13.25	−259.14	14.15	−57.64	21.62
ΔG_{vdW}	−24.42	3.17	−56.04	5.04	−64.89	6.26
ΔG_{np}	−2.19	0.38	−7.74	0.27	−7.56	0.58
ΔG_{PB}	83.68	12.79	263.80	11.20	110.71	16.20
ΔG_{cavity}	−2.19	0.38	−7.74	0.27	−7.56	0.58
ΔG_{gas}	−97.82	13.49	−315.17	12.93	−122.52	19.55
ΔG_{sol}	81.50	12.66	256.06	11.16	103.14	16.32
$-T\Delta S_{tot}$	17.36	12.94	35.71	8.86	36.67	7.40
ΔG_{bind}[a]	−16.33	3.66	−59.12	6.07	−19.38	6.734
ΔG_{bind}[b]	1.03	–	−23.41	–	17.29	–

All values are given in kcal/mol.
[a] The predictions of binding energy do not include entropy effect.
[b] The predictions of binding energy include entropy effect.

After introduction of the conformational entropy ($-T\Delta S_{tot}$), the absolute binding free energies for CPBHz–PCI, CPAHa–PCI and CPBh–PCI become 1.03, −23.41 and 17.29 kcal/mol, respectively. The absolute binding free energies of CPAHa–PCI and CPBh–PCI deviate from the experimental values, which might be due to the inaccurate estimation of entropies, as reported in other protein complexes (Deng and Cieplak, 2009; Zoete and Michielin, 2007). It is worth noting that the standard deviation (std) of entropy for CPBHz–PCI is very large (Table 1), which mainly arises from the high oscillation of the vibrational entropy (data not shown). This is reasonable as demonstrated by the highly unstable characteristics of the system (see Fig. 2). Additionally, the normal-mode methodology does not incorporate the configurational entropy associated with multiple energy minima and with transitions therein, possibly leading to an incomplete representation of the entropic cost for binding (Chang et al., 2007).

3.1.3. Binding mode of MCP-PCI complex

To reveal the differences in structural basis of the PCI-insensitive/-sensitive binding patterns, the three complexes are extensively investigated, which were taken from the representative snapshot of the last 1 ns MD trajectory (Fig. 4).

Fig. 4A and C show that PCI adopts a similar global conformation binding to CPAHa and CPBh, with its C termini penetrating into the active site of CPBHz/CPBh. The C termini of PCI nestles in the groove of CPAHa characterized by residues Glu69, Arg71, Asp163, Thr164, Ser197, Phe198 and Glu270 (Fig. 4A). The coordination bond formed between Val38i and zinc ion, as well as the H-bonding and hydrophobic interactions strongly stabilize the complex, suggesting the potent binding of PCI to CPAHa. Fig. 4C depicts that the C termini of PCI is lodged in the active pocket surrounded by residues Arg71, Arg127, Arg145, Thr164, Tyr198, Thr248 and Phe279 via H-bonding, hydrophobic and π–π interactions. Different from the CPAHa–PCI complex, the C termini of PCI is anchored at the entrance via H-bonds, which hinders its deep access to the active-site groove of CPBh. This explains why PCI weakly inhibited CPBh function (Arolas et al., 2005). Fig. 4B reveals that PCI is far away from CPBHz, as reflected by the distance between the carboxyl group of Val38i and zinc ion (~19.7 Å), indicating the two molecules are not bounded by bounds. This is also evidenced by the positive binding free energy (1.03 kcal/mol) of the complex.

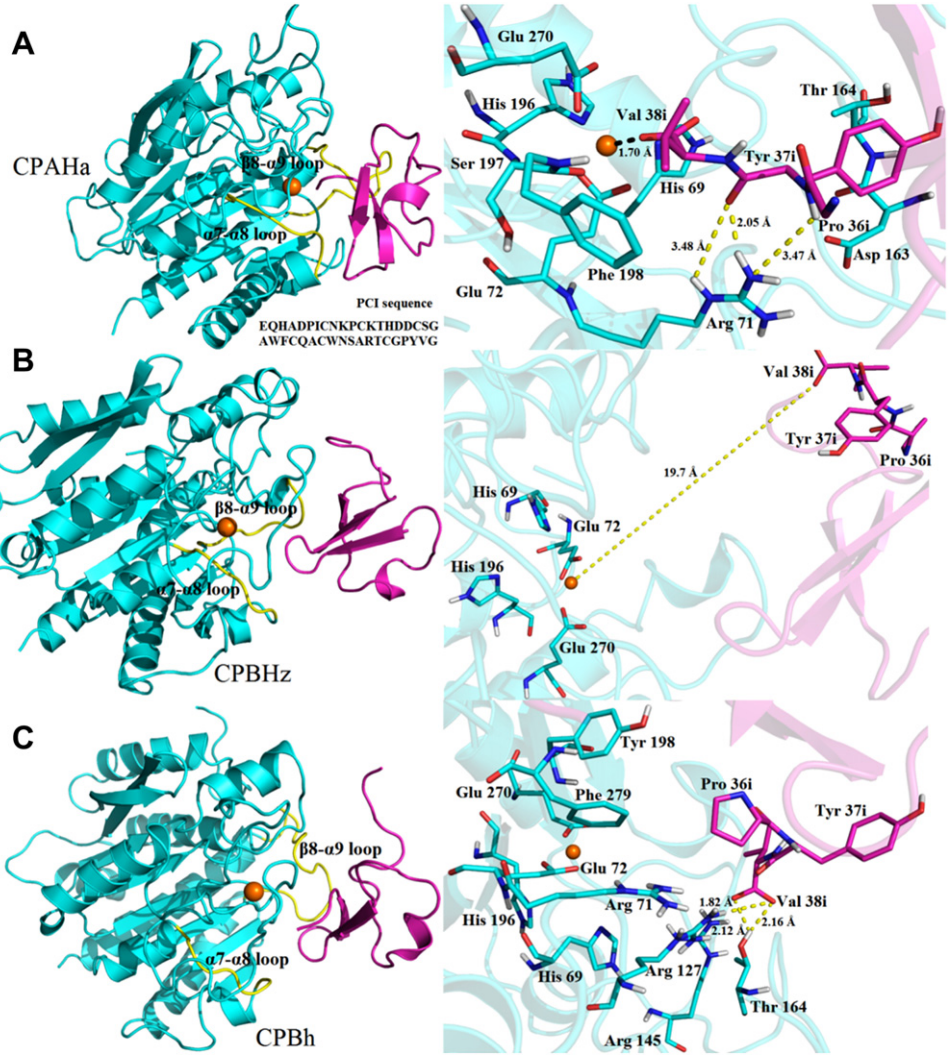

Fig. 4. Putative binding of PCI (sticks model) in the active site of (A) CPAHa, (B) CPBHz and (C) CPBh (only residues in a shell at a distance <4.5 Å from the inhibitor are shown). H-bonds are depicted as dashed lines (see the text for details). Some residues relevant for catalysis or binding are labeled. The figure is colored in atom type representation: green (carbon), red (oxygen), orange (sulfur), white (hydrogen) and blue (nitrogen). The zinc is depicted as a orange sphere. Non-polar hydrogen atoms were hided for clear. (For interpretation of the references to colour in this figure legend, the reader is referred to the web version of this article.)

3.1.4. Free energy decomposition

To understand the MCP–PCI interactions in depth, the total binding free energies were decomposed per residue with MM/GBSA approach. The results are shown in Fig. 5 and the contributions of key residues ($|\Delta G| > 1.0$ kcal/mol) are listed in Table 2.

Fig. 5A shows that 60% residues of CPAHa in binding surface, i.e., Phe125, Arg127, Phe244, Val246, Leu247, Tyr248, Asn273, Ser274, Val275, Trp276, Phe277 and Phe279, contribute with more than 1 kcal/mol to the total binding free energy, which is in accordance with the H-bonding network and hydrophobic interactions in the CPAHa–PCI complex (see section 3.1.3). On the contrary, residues Glu72 and Glu270 offer unfavorable energy (+1.90 and +3.08 kcal/mol, respectively). This is a consequence of a close contact between Glu72 and Glu270, resulted from the unique coordination bond established between Val38i and zinc ion, stabilizing the complex structure. Fig. 5B depicts that only 12% residues (Ser276, Gly277 and Trp278) of the CPBHz in binding surface make significant favorable contributions (<−1.00 kcal/mol) to the binding free energy. It is interesting to note that these residues reside in the β8-α9 loop (residues 272–286), which is similar to that of CPAHa–PCI complex. Table 2 reports that the favorable binding free energies of those residues are mainly from van der Waals and electrostatic energies, due to the interactions established between these residues and PCI. Fig. 5C displays that 20% residues (Phe125, Arg127, Gly275, Tyr277 and Phe279) of the CPBh in binding surface contribute remarkably to the binding free energy. Among them, Gly275, Tyr277 and Phe279 in CPBh–PCI complex are located in β8-α8 loop, similarly to the other two complexes. The prominent contribution of Arg127 and other residues are mainly from electrostatic energy and van der Waals energy, as suggested in Table 2.

To acquire more quantitative information of these complexes, the differences in the key residue contributions were analyzed.

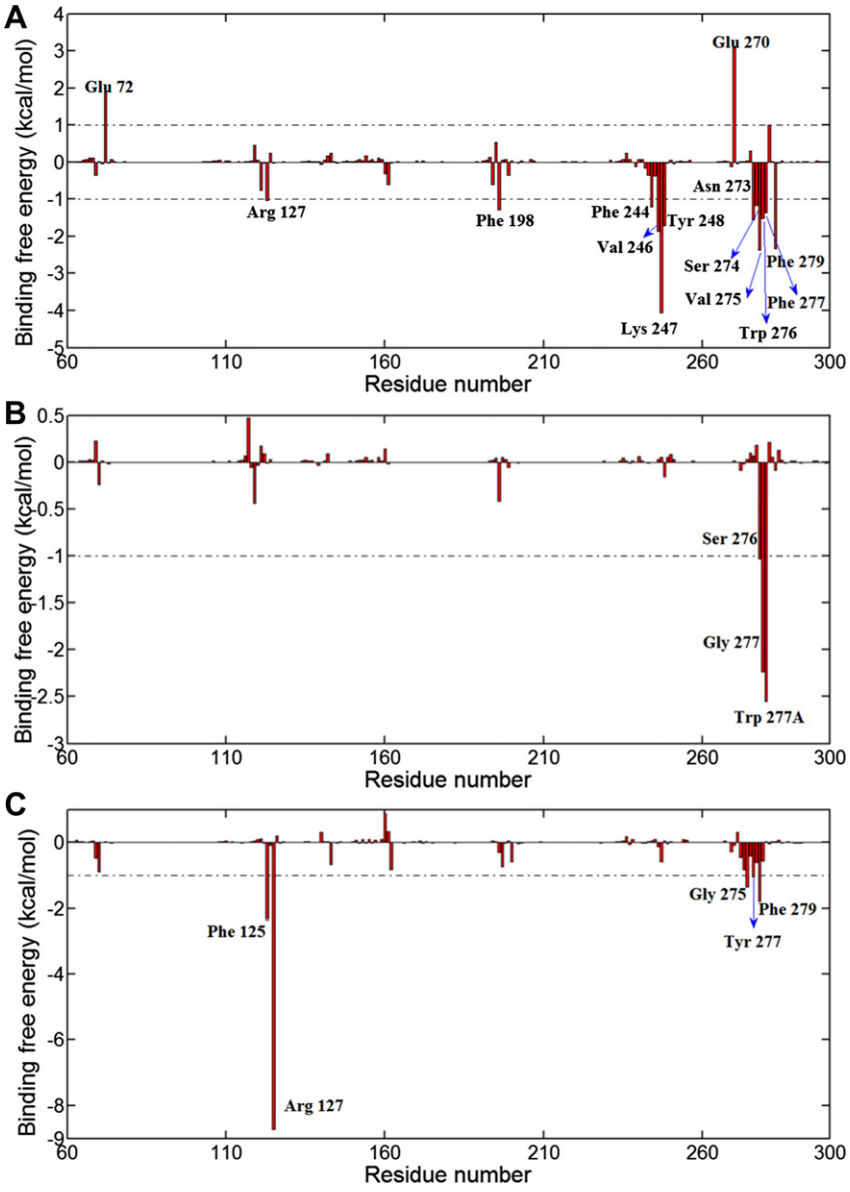

Fig. 5. Residue–residue interaction spectrums of (A) the CPAHa–PCI complex, (B) the CPBHz–PCI complex and (C) the CPBh–PCI complex according to the MM/GBSA method. The *x*-axis denotes the residue number of MCPs and the *y*-axis denotes the interaction energy between the PCI and MCPs residues. The important residues for binding are marked by corresponding texts. Residues 1–59 and residues after 300 in each enzyme were ignored in that these residues were not involved in the interactions between MCP and PCI and their energy contribution can be negligible (<0.001 kcal/mol).

Table 2
Decomposition of ΔG on a per-residue basis.[a]

Residue	S_{vdw}	B_{vdw}	T_{vdw}	S_{ele}	B_{ele}	T_{ele}	S_{GB}	B_{GB}	T_{GB}	T_{GBSUR}	T_{GBTOT}
CPBHz-PCI											
Ser276	−1.13	−1.06	−2.19	−0.94	−1.82	−2.76	2.53	1.81	4.34	−0.42	−1.03
Gly277	0.00	−1.48	−1.48	0.00	−3.72	−3.72	0.00	3.33	3.33	−0.37	−2.24
Trp277A	−2.61	−0.58	−3.19	−0.49	−1.38	−1.87	1.80	1.34	3.13	−0.62	−2.55
CPAHa–PCI											
Glu72	0.33	−0.04	0.29	41.01	0.99	42.01	−39.36	−0.99	−40.35	−0.04	1.90
Arg127	−1.50	−0.06	−1.56	−26.41	0.89	−25.53	27.04	−0.82	26.23	−0.17	−1.03
Phe198	−1.65	−0.99	−2.65	0.06	1.94	1.99	0.38	−0.60	−0.22	−0.41	−1.29
Phe244	−0.40	−0.13	−0.52	−0.34	−4.26	−4.60	0.37	3.68	4.05	−0.13	−1.20
Val246	−0.61	−1.52	−2.13	0.70	−5.42	−4.72	−0.36	5.65	5.29	−0.31	−1.87
Leu247	−2.40	−1.94	−4.34	−0.50	−4.37	−4.87	0.87	5.06	5.93	−0.76	−4.05
Tyr248	−1.59	−0.49	−2.08	−0.62	0.50	−0.12	1.28	−0.45	0.83	−0.35	−1.72
Glu270	−0.19	−0.06	−0.26	37.70	0.22	37.92	−34.25	−0.25	−34.49	−0.08	3.08
Asn273	−0.13	0.13	0.00	−2.10	−4.53	−6.63	2.15	3.02	5.17	−0.08	−1.55
Ser274	−0.11	−0.46	−0.58	1.20	−9.14	−7.94	−1.03	8.60	7.57	−0.22	−1.17
Val275	−0.60	−1.28	−1.89	2.40	−7.90	−5.50	−2.07	7.49	5.42	−0.40	−2.37
Trp276	−0.52	−1.28	−1.80	−0.53	−2.86	−3.39	0.59	3.22	3.81	−0.13	−1.51
Phe277	−0.70	−0.56	−1.27	0.35	−0.76	−0.41	−0.13	0.68	0.54	−0.23	−1.37
Phe279	−2.04	−0.12	−2.16	−1.04	0.21	−0.82	1.08	−0.12	0.96	−0.31	−2.33
CPBh–PCI											
Phe125	−2.26	−0.48	−2.74	−0.22	0.59	0.36	1.02	−0.40	0.62	−0.59	−2.35
Arg127	−0.17	−0.06	−0.23	−45.15	0.01	−45.13	36.78	0.06	36.84	−0.20	−8.72
Gly275	0.00	−2.44	−2.44	0.00	−0.43	−0.43	0.00	1.94	1.94	−0.43	−1.36
Tyr277	−0.21	−1.00	−1.21	−0.06	−0.72	−0.79	0.05	0.98	1.04	−0.08	−1.04
Phe279	−1.75	−0.23	−1.98	−0.10	−0.35	−0.45	0.44	0.56	1.00	−0.37	−1.80

[a] Energies shown as contributions from van der Waals energy (vdW), electrostatic energy (ele), polar solvation energy (GB) and the non-polar solvation energy (SUR) of side chain atoms (S), backbone atoms (B), and the sum of them (T) of MCP–PCI complexes. Only residues of $|\Delta G| > 1.0$ kcal/mol were listed. All values are given in kcal/mol.

According to Table 2, residues Arg127, Phe277/Tyr277 and Phe279 all contribute significantly to the binding free energies of CPAHa–PCI and CPBh–PCI complexes, inferring that these residues are essential for PCI binding to MCPs. Furthermore, the much smaller contribution of the seven residues (Phe125, Arg127, Phe198, Phe244, Val246, Leu247 and Tyr248) in CPBh–PCI complex than those in CPAHa–PCI complex may explain the high selectivity of PCI to CPAHa and CPBh.

3.1.5. The mechanism of PCI-resistance

In order to interpret the difference in binding modes, we closely inspect the structures of these three enzymes along the MD simulations and find that: 1) the β8-α9 loop in CPBHz protrudes toward the active site, which is completely different from that in other MCPs. In details, the indole group of Trp277A in CPBHz directs toward the active site cleft during the MD simulations process, shading the entrance to the active site of CPBHz. While the side chain of the corresponding residue in CPAHa (Phe277) and CPBh (Trp277) structures extends outward of the active site over the entire simulations process and thus open the entrance to PCI. This shows a convincing consistency with Bayés A. et al.'s work (Bayés et al., 2005) and confirms that the orientation of the side chain of residue in position 277 is critical to determine whether MCP is sensitive or insensitive to PCI. 2) The insertion of Gly247A leads to a subtle local change of the α7-α8 loop, which makes Gly247A and its both side residues Ile247 and Tyr248 stay ~3 Å away from the active site as compared with the corresponding residues (Leu247 and Tyr248) in the CPAHa structure. Thus, the H-bonds that established in the Leu247–Asn29i and Leu247–Ser30i of other two complexes disappear in CPBHz–PCI complex. This result implies that the insertion of Gly247A weakens the stabilization of CPBHz and PCI. 3) The distances between the loops β8-α9 and α7-α8 (colored yellow in Fig. 4) which provide a funnel-like access to the active sites, in the two proteins seems to be similar (~23 Å), as evidenced by conserved residues Tyr248 (OH) and Phe279 (CB). However, this entrance of CPBHz is narrowed down to ~12 Å by the large inner-extended indole moiety of Trp277A, blocking the entering of PCI. These findings indicate that the "gatekeeper" Trp277A plays a major role in the adaption of CPBHz to PCI, which clearly clarifies the resistant mechanism of CPBHz to PCI.

3.2. MCP–THI complex

3.2.1. Global structure behavior

The RMSD of the backbone atoms of the starting structures over the simulated time shows that the three MCP–THI complexes all give the RMSD values converged below 1.5 Å, which means the MD trajectories of the complexes appear to be well equilibrated after approximately 1 ns of the simulation (Fig. 6). We observe that the RMSD curves of CPBHz–THI and CPAHa–THI complexes are more steady with relatively low RMSD values (below 1.2 Å) than that of CPBh–THI complex (~1.5 Å). The trajectory demonstrates that the relatively large oscillation of CPBh–ligand complex is resulted from two high flexible loop regions (Ala1 ~ Trp12 and Lys119 ~ Lys171), as compared with the other two complexes. From this, it is inferred that THI binds to CPBHz and CPAHa more tightly than to CPBh.

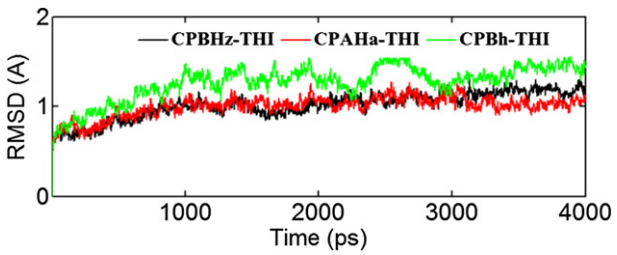

Fig. 6. Root-mean-square deviation (RMSD) of the backbone atoms (C, N, and C_α) of the CPBHz–PCI complex, the CPBHa–PCI complex and the CPBh–PCI complex with respect to the first snapshot as a function of time.

In order to examine the fluctuations, the backbone RMSF of each residue from its time-average position is depicted in Fig. 7. Overall, the protein structures of all complexes share similar RMSF distributions and dynamic features. The average RMSFs for the CPBHz–THI, CPAHa–THI and CPBh–THI complexes are 0.59 Å, 0.83 Å and 0.57 Å, respectively. As a whole, α helices and β sheets show a rigid behavior in the enzymes, and the loops show relatively greater fluctuations, especially for residues 87–90 (in the α2-α3 loop) in CPBHz. Similarly, the residues near the two ends of the MCPs exhibit relatively high flexibility except the C-terminal of CPBh and N-terminal of CPAHa just like the MCP–PCI system. The above observation can be easily explained by the binding between protease and inhibitor that leads directly to the rigidity of the complex.

3.2.2. Binding free energy

To compare the binding affinity of THI with CPBHz, CPAHa and CPBh, the binding free energies of the three MCP–THI systems were calculated by MM/PBSA method with single trajectory protocol. The predicted binding affinities and the energy components of the three complexes are listed in Table 3. Because the experimental data for only two of the three complexes are available, our comparison with experiments involves only the two interactions. According to Table 3, the rank of the ΔG_{bind} values for the three complexes is −16.44 kcal/mol (CPBh–THI complex) > −20.05 kcal/mol (CPBHz–THI compex) > −31.14 kcal/mol (CPAHa–THI complex), corresponding to a decrease in the binding affinity without considering the entropy effect. This is in line with the reported data (Fernández et al., 2009a), which indicate that the K_i value of THI against CPBh (1.6 μM) is about 3-fold higher than that of THI against CPBHz (0.58 μM).

To determine which energy term makes the most favorable contributions, a detailed analysis of the binding free energy components (ΔE_{ele}, ΔG_{vdw}, ΔG_{np} and ΔG_{PB}) was performed. As suggested in Table 3, the electrostatic term (ΔE_{ele}) in the gas phase provides the major favorable contribution to the inhibitor binding, in which the electrostatic interaction of the CPAHa–THI complex (−97.36 kcal/mol) is relatively stronger than those of the other two complexes (−89.71 and −72.66 kcal/mol for CPBHz–THI and CPBh–THI, respectively). Similarly, the van der Waals contribution is also favorable for the binding between THI and MCPs and contributes similarly in these three complexes (−28.30, −24.19 and −28.10 kcal/mol for CPAHa–THI, CPBHz–THI and CPBh–THI, respectively). Non-polar solvation energies (ΔG_{np}) also contribute slightly favorably. However, considering the polar solvation contribution (ΔG_{PB}), which could counteract the electrostatic interaction (ΔE_{ele}), the net electrostatic contributions ($\Delta E_{ele} + \Delta G_{PB}$) of the three complexes are unfavorable for the binding (7.71, 0.72 and 15.38 kcal/mol for CPAHa–PCI, CPBHz–THI and CPBh–THI, respectively). It can be concluded that the electrostatic energy is the main driving force of the binding for THI to MCPs (70%). And the calculated difference in electrostatic interaction could explain the different binding affinity of THI to CPBHz, CPAHa and CPBh.

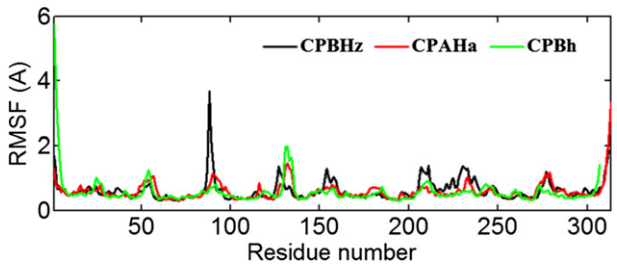

Fig. 7. Root-mean-square fluctuation (RMSF) of backbone atoms versus residue number of the CPBHz–THI, CPAHa–THI and CPBh–THI complexes over the course of each 4 ns simulation.

Table 3
Binding free energy estimates for MCP–THI complexes.

Contribution	CPBHz–THI		CPAHa–THI		CPBh–THI	
	Mean	Std	Mean	Std	Mean	Std
ΔE_{ele}	−89.71	7.08	−97.36	8.39	−72.66	6.46
ΔG_{vdW}	−24.19	4.03	−28.30	3.97	−28.10	3.84
ΔG_{np}	−3.57	0.18	−3.66	0.11	−3.72	0.13
ΔG_{PB}	97.42	7.95	98.18	5.70	88.04	6.99
ΔG_{cavity}	−3.57	0.18	−3.66	0.11	−3.72	0.13
ΔG_{gas}	−113.89	6.09	−125.66	7.50	−100.76	5.93
ΔG_{sol}	93.85	7.88	94.52	5.65	84.32	6.95
$-T\Delta S_{tot}$	16.28	11.09	19.38	8.49	19.41	9.07
ΔG_{bind}[a]	−20.05	7.35	−31.14	5.96	−16.44	6.27
ΔG_{bind}[b]	−3.77	–	−11.76	–	2.97	–

[a] The predictions of binding energy do not include entropy effect.
[b] The predictions of binding energy include entropy effect.

When the entropy term is added, the binding free energies for CPBHz–THI, CPAHa–THI and CPBh–THI complexes are −3.77, −11.76 and 2.97 kcal/mol, respectively. Entropy terms ($-T\Delta S_{tot}$) produce unfavorable contributions to the binding of THI to MCPs. Table 3 indicates that the std for CPBHz–THI complex is very large (11.09), which mainly arises from the high std value of vibrational entropy (data not shown). The vibrational entropy with a large std value is probably induced by the dramatically swing of the methylquinolin and thiophene groups of THI in CPBHz. Discrepancy between the computed and experimental absolute binding free energy of CPBHz–THI complex may attribute to the inaccurate estimation of entropy.

3.2.3. Binding mode of MCP–THI complex

To probe how the specific active site residues influence the relative binding affinities, the binding mode of MCP–THI complex is extensively investigated to complement the energy analyses. As observed in Fig. 8, the binding modes of the three complexes are similar: THI locates in the S1′, S1 and S2 domains of MCPs, which is in good agreement with the MCP-bound crystallographic studies (Adler et al., 2008; Fernández et al., 2009a, b).

Fig. 8A reveals that THI is anchored at the active site of CPBHz with its methylquinolin group toward the inside pocket. In this pocket, five H-bonds are established between THI and residues Arg127, Asn144, His196 and Tyr248, as highlighted in Fig. 8A. Furthermore, the benzene ring of methylquinolin group of THI forms π-cation interaction with Arg145. Prominently, the carbonyl oxygen of THI forms a strong coordination bond with the catalytic zinc ion (∼2.0 Å). A crystal water molecule W3644 also stabilizes the binding by mediating the interaction between THI and Glu270, Glu72 and Ser197. Interestingly, in CPAHa–PCI and CPBh–PCI complexes, the methylquinolin group of THI is orientated toward outside of the pocket (Fig. 8B and C), rotating nearly 180° as compared with that in CPBHz structure. Instead, both benzene ring and thiophene ring of THI form π-cation interactions with Arg145 in CPAHa–PCI and CPBh–PCI complexes. However, considering the nature of the π system and the interaction geometry, the π-cation interaction in CPAHa–PCI is the most potent, followed by CPBHz–PCI and CPBh–PCI. Like the THI binding to CPBHz structure, the same coordination bond and similar H-bonds and crystal waters are also observed in CPAHa–PCI and CPBh–PCI complexes (see Fig. 8B and C).

By comparing the binding modes, the main difference in THI binding to insect and human MCPs is resulted by the critical

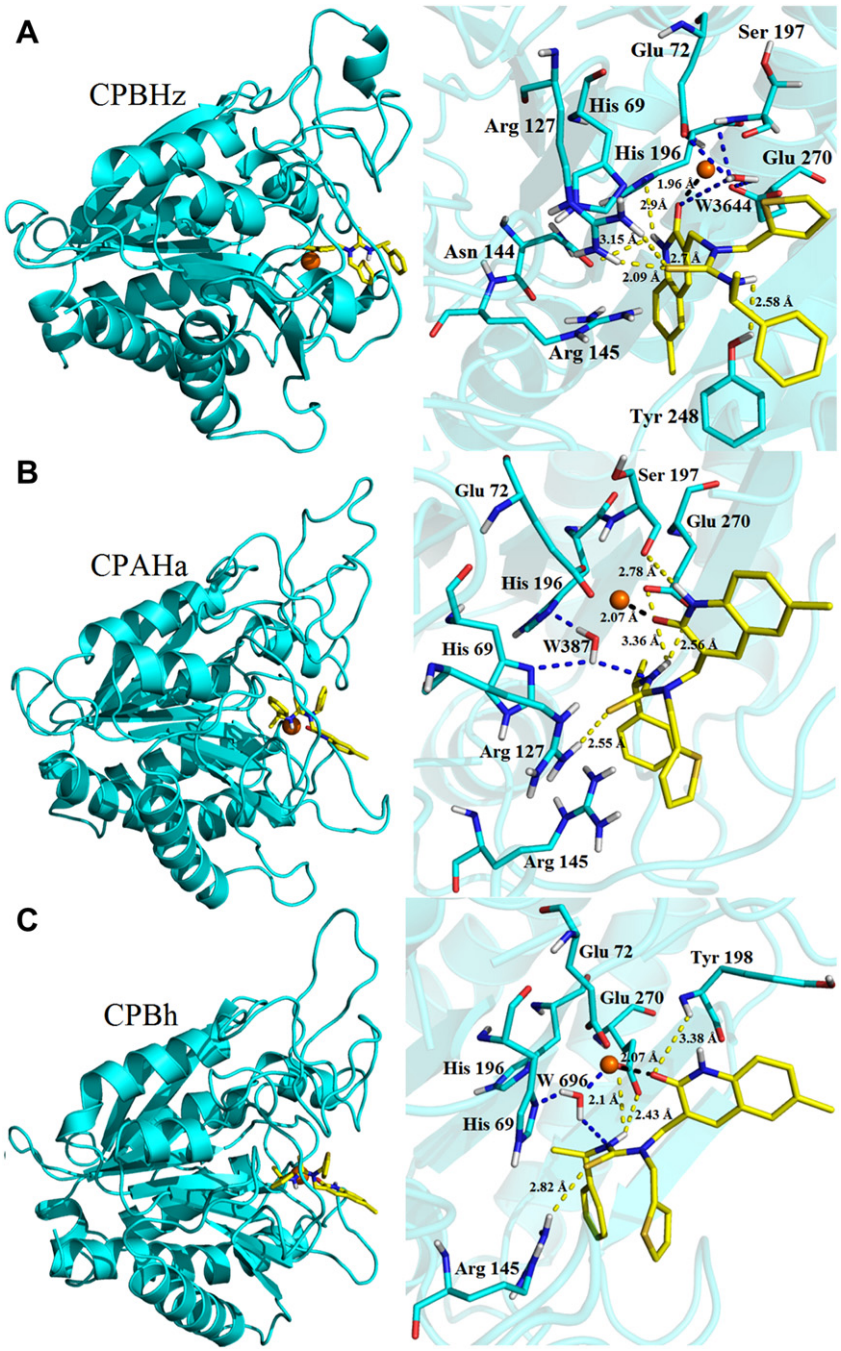

Fig. 8. Putative binding of THI (sticks model) in the active site of (A) CPBHz, (B) CPAHa and (C) CPBh (only residues in a shell at a distance <4.5 Å from the inhibitor are shown). H-bonds are depicted as dashed lines (see the text for details). Some residues relevant for catalysis or binding are labeled. The figure is colored in atom type representation: green (carbon), red (oxygen), orange (sulfur), white (hydrogen) and blue (nitrogen). The zinc is depicted as a orange sphere. Non-polar hydrogen atoms were hided for clear. (For interpretation of the references to colour in this figure legend, the reader is referred to the web version of this article.)

H-bond related with the C═S part of THI. In the CPBHz–THI and CPAHa–THI complexes, this S will form H-bond with Arg127 and thus tightly locks THI in the inner active site. However, the same S builds H-bond with Arg145 in CPBh–THI complex, thus keeping THI in outer active site. This is consistent with the binding free energy calculations and explains why THI exerts more potency against insect MCPs than human one.

3.2.4. Free energies decomposition

To identify the key residues related to the binding process, a per-residue decomposition of the total binding free energy of each complex was performed using MM/GBSA method and the results were displayed in Fig. 9. The contributions of key residues ($|\Delta G| > 1$ kcal/mol) from different energy terms are also listed in Table 4.

Overall, the interaction spectrums of the three complexes have similar features. In Fig. 9A, residues Glu72, Arg127, His196, Ser197, Ile245 and Glu270 are mainly responsible for THI binding to CPBHz, accounting for 24% residues of CPBHz in interaction surface. According to Table 4, the electrostatic and polar solvation energies are dominant favorable contributions to the binding, which is in accordance with the H-bonding and π-cation interactions

established between THI and CPBHz. Fig. 9B indicates that seven residues (Glu72, Arg127, Arg145, Ile243, Leu247, Glu270 and Phe279) contribute most to the binding free energy of CPAHa–THI complex, especially Glu72, Arg145, Leu247 and Glu270 (≥2 kcal/mol). For residues Glu72, Arg127 and Arg145, the electrostatic energy and the Polar solvation energy are the major force that drives the binding of THI to CPAHa (see Table 4), which is in consistent with the H-bonding networks formed in this complex. While for residues Ile243, Leu247, Glu270 and Phe279, van der Waals energy dominates the binding. In Fig. 9C, four residues Glu72, Arg145, Ile245 and Glu270 contribute most to the binding of THI to CPBh. Among them, only the contribution of residue Glu72 is more than 2.0 kcal/mol. Seen from Table 4, the main binding driving force for these residues are the electrostatic and polar solvation energies.

To conclude, both Glu72 and Glu270 make large contributions to the binding free energy in the three complexes, implying that these two residues are vital for the binding. Furthermore, the number of great contributor (>2.0 kcal/mol) residues for CPBHz–THI, CPAHa–THI and CPBh–THI complexes is 2, 4 and 1, respectively. This also indicates that THI can produce the strongest binding affinity with CPAHa.

3.3. Other MCP-small molecular inhibitor complexes

To improve our understanding of the selectivity of small molecular inhibitor to MCPs, the binding affinities and binding modes of other three compounds, i.e. DF5, DF4, BSA (Supporting information Figure S1), derived from different families (Fernández, 2009; Fernández et al., 2009b) bound to CPBHz/CPAHa/CPBh were also investigated.

3.3.1. Global structure behavior

To explore the dynamic stability of complexes and to ensure the rationality of the sampling method, RMSD from the starting

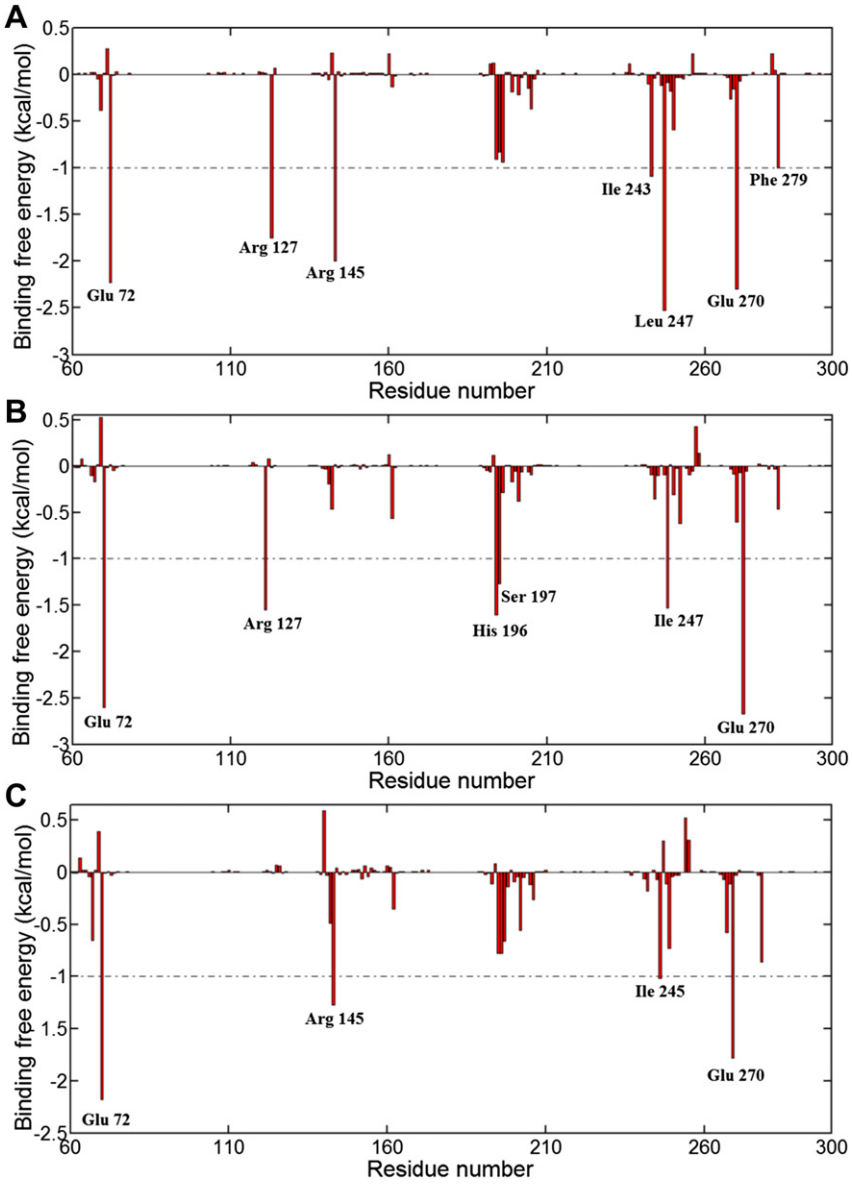

Fig. 9. Residue-ligand interaction spectrum of (A) the CPBHz–THI complex, (B) the CPBh–THI complex and (C) the CPAHa–THI complex according to the MM/GBSA method. The *x*-axis denotes the residue number of MCPs and the *y*-axis denotes the interaction energy between the PCI and MCPs residues. The important residues for binding are marked by corresponding texts. Residues 1–59 and residues after 300 in each enzyme were ignored in that these residues were not involved in the interactions between MCP and PCI and their energy contribution can be negligible (<0.001 kcal/mol).

Table 4
Decomposition of ΔG on a per-residue basis.[a]

Residue	S_{vdw}	B_{vdw}	T_{vdw}	S_{ele}	B_{ele}	T_{ele}	S_{GB}	B_{GB}	T_{GB}	T_{GBSUR}	T_{GBTOT}
CPBHz–THI											
Glu72	−0.61	−0.02	−0.63	8.38	0.09	8.47	−10.36	−0.07	−10.42	−0.02	−2.60
Arg127	−0.30	−0.03	−0.33	−11.16	0.17	−10.99	10.12	−0.12	10.00	−0.23	−1.55
His196	−1.16	−0.08	−1.24	−0.02	−0.41	−0.43	−0.50	0.61	−0.11	−0.04	−1.60
Ser197	−0.02	−0.22	−0.24	0.13	0.82	0.95	−0.28	−1.70	−1.98	0.00	−1.27
Ile247	−1.27	−0.20	−1.47	0.25	−0.19	0.06	−0.26	0.38	0.11	−0.23	−1.53
Glu270	−1.34	−0.06	−1.40	3.19	−0.17	3.02	−4.37	0.25	−4.12	−0.17	−2.67
CPAHa–THI											
Glu72	−0.62	−0.03	−0.65	9.73	0.13	9.86	−11.26	−0.14	−11.40	−0.04	−2.23
Arg127	−0.53	−0.02	−0.55	−11.87	0.30	−11.56	10.74	−0.27	10.48	−0.11	−1.75
Arg145	−1.14	−0.03	−1.17	−11.45	0.12	−11.33	10.71	0.00	10.70	−0.20	−2.00
Ile243	−0.75	−0.15	−0.90	0.02	−0.29	−0.28	−0.06	0.27	0.21	−0.13	−1.09
Leu247	−1.96	−0.26	−2.22	0.14	0.02	0.16	−0.07	−0.01	−0.08	−0.38	−2.53
Glu270	−1.66	−0.09	−1.75	0.73	−0.29	0.44	−1.11	0.30	−0.81	−0.18	−2.30
Phe279	−0.90	−0.05	−0.95	−0.31	0.09	−0.22	0.41	−0.09	0.33	−0.16	−1.00
CPBh–THI											
Glu72	−0.56	−0.03	−0.59	9.21	0.15	9.36	−10.80	−0.12	−10.92	−0.04	−2.18
Arg145	−1.69	−0.05	−1.74	−10.77	0.12	−10.65	11.38	0.02	11.40	−0.29	−1.27
Ile245	−0.73	−0.08	−0.81	0.14	0.01	0.15	−0.17	−0.03	−0.20	−0.16	−1.02
Glu270	−1.46	−0.08	−1.54	−1.05	−0.24	−1.29	1.02	0.27	1.30	−0.24	−1.78

[a] Energies shown as contributions from van der Waals energy (vdW), electrostatic energy (ele), polar solvation energy (GB) and the non-polar solvation energy (SUR) of side chain atoms (S), backbone atoms (B), and the sum of them (T) of MCP–THI complexes. Only residues of $|\Delta G| > 1.0$ kcal/mol were listed. All values are given in kcal/mol.

structure are analyzed (Supporting information Figure S2). After 4 ns MD simulations, the RMSD of each complex tends to converge at ~1.5 Å, indicating the systems are stable. Furthermore, analyses of RMSF versus the residue number for complexes are illustrated in supporting information Figure S3. On the whole, these nine complexes share similar RMSF profiles and dynamic features, similar to those of MCP–THI complexes. The average RMSFs for the CPBHz–DF5, CPAHa–DF5, CPBh–DF5, CPBHz–DF4, CPAHa–DF4, CPBh–DF4, CPBHz–BSA, CPAHa–BSA, and CPBh–BSA complexes are 0.54 Å, 0.60 Å, 0.68 Å, 0.74 Å, 0.61 Å, 0.69 Å, 0.72 Å, 0.58 Å, and 0.60 Å, respectively. The relatively larger RMSFs of CPBHz–DF4 and CPBHz–BSA complexes may be explained by the relatively weaker binding between them.

3.3.2. *Mechanisms of binding and selectivity for inhibitors*

The binding free energies calculated for the three compounds with MCPs by MM/PBSA method are summarized in supporting information Table S1-S3.

MCP–DF5 complex. The predicted binding free energies of DF5 with CPBHz, CPAHa and CPBh are −29.60, −6.46 and −25.00 kcal/mol, respectively (Table S1). This is consistent with the experimental data (Fernández, 2009), which indicates that DF5 is more potent against CPBHz (K_i: 0.42 μM) than CPBh (K_i: 8.0 μM). The major favorable contributions to binding are electrostatic and van der Waals energies, whereas polar solvation energy opposes the binding. Further examination reveals that the electrostatic energy in CPBHz–DF5 (−76. 21 kcal/mol) and CPBh–DF5 (−82.70 kcal/mol) is larger than that of CPAHa–DF5 (−36.63 kcal/mol). The entropic contributions of these three complexes disfavor the binding with positive values (Table S1). And the unstable binding further results in the large irrational vibration entropy (data not shown). According to the binding modes of the complexes shown in Figure S4, DF5 binds well to the active site of the CPBHz and CPBh through strong coordination bond, H-bonds and π–π interactions. However, due to the loss of the coordination bonds between zinc and DF5, compound DF5 is not well bound to CPAHa.

MCP–DF4 complex. The binding free energy analysis indicates that the electrostatic, van der Waals and polar solvation energies constitute the major part of enthalpy in the three complexes. Among them, electrostatic and van der Waals energies favor DF4 binding to MCP, whereas Polar solvation energy disfavors this binding. The entropy also opposes binding and scale up binding free energies by about 20 kcal/mol. According to Table S2 and Figure S5, DF4 does not bind well with CPBHz and CPBh, as demonstrated by their binding free energies (−1.27 kcal/mol and 8.00 kcal/mol, respectively). However, DF4 binds well to CPAHa through strong coordination bond and several H-bonds, in agreement with the binding free energy (−27.86 kcal/mol).

MCP–BSA complex. Plus the entropy contributions, the absolute binding free energies for CPBHz–BSA, CPAHa–BSA, CPBh–BSA complexes are 20.90, 8.83 and −8.57 kcal/mol, respectively. In all the cases, the binding is driven by favorable electrostatic and van der Waals contributions, while polar solvation and entropy terms oppose binding. Figure S6 depicts that BSA is anchored in the active site of CPBh by some H-bonds and two coordination bonds formed between the nitrogen atoms of oxadiazole ring and zinc ion. While in CPBHz–BSA and CPAHa–BSA complexes, the coordination bond disappeared and few H-bonds are formed. This is in line with the binding free energy result.

All these results demonstrate that some small molecules might not be species-specific inhibitors, like BSA, which is selectively against human MCP. Thus, more attention should be paid in the design of selective inhibitors for insect MCP.

3.4. *Insights for future design of novel inhibitors*

As far as we know, researches about plant PIs of insect MCPs are extensively conducted, while the synthesized inhibitors against insect MCPs studies are few. In this work, the study of the PCI/THI against MCPs by MD simulations, binding free energy and energy decomposition methods offers valuable and deep perspectives on the detailed interactions of MCPs with the natural peptide inhibitor and synthetic small molecule inhibitors. Energy analyses reveal that the electrostatic energy and the van der Waals energy are both critical for the favorable binding free energies of PCI–MCP complexes and THI–MCP complexes, especially the electrostatic one. But these two energy terms in the

MCP–PCI complexes are stronger than those in the MCP–THI complexes. Moreover, the binding free energy analyses suggest that the selectivity of PCI to insect MCP and human MCP is better than that of THI. The binding modes and binding free energy decompositions of these two systems show that residues Glu72, Arg127, Leu247, Glu270 and Phe279 are of importance to inhibit against the insect CPA whether natured or synthesized. This indicates that new potent inhibitors can be designed by enhancing the interactions with these residues. Furthermore, the computational results discussed above have demonstrated some important findings: (1) the coordination bond formed between zinc ion and inhibitor is necessary for inhibitor exerting the inhibitive interaction; (2) H-bonds established between inhibitors and residues Glu72, Arg127 and Leu247 play vital roles in stabilizing the complexes; (3) π-cation interactions established between THI and Arg127/Arg145 in MCP–THI complexes as well as hydrophobic interactions formed between Tyr248 and Tyr37i/Val38i in MCP–PCI complexes are important for enhancing the inhibitive interaction.

4. Conclusion

In the present study, to clarify the resistant mechanism of insect carboxypeptidase against potato protease inhibitor and explore the selectivity of PCI and THI to human and insect MCPs, MD simulations, MM/PBSA free energy calculations, and MM/GBSA free energy decomposition analysis were conducted. The results show that the predicted binding free energy of the insect PCI-sensitive complex is more favorable than that of the PCI-insensitive mutant, which indicates that the insertion of Gly247A and substitution of Tyr277 (Trp277A) are unfavorable for the PCI binding to CPBHz, in accordance with the experimental data. The estimation of the contributions of individual energy terms to binding free energy demonstrates that the major contribution to the binding of MCP and PCI is the electrostatic energy component, affecting the differences of binding affinity among the three MCPs. The analysis also shows that the resistance of CPBHz is mainly due to the loss of electrostatic energy component, as reflected by the disappearing of some important H-bonds. According to the structural analysis, residues Gly247A and Trp277A of CPBHz alter the secondary binding site formed by β8-α9 loop and α7-α8 loop, leading to conformational change of the access to the active site and blocking the entrance of PCI. Moreover, based on the free energy decomposition analysis, the difference of the binding free energy is primarily determined by seven residues (Glu72, Phe198, Val246, Leu247, Tyr248, Asn273 and Ser274) of MCP in PCI–MCP complexes and two residues (Arg145, Leu247) of MCP in THI–MCP complexes, respectively. All these residues established important interactions between MCPs and inhibitors.

In summary, the findings in this work could provide a better structural explanation for the deep understanding of PCI-resistant mechanism of insect MCP and give clues for PCI mimic design to protect agronomically important crops from pest infestation. In addition, the information of inhibition mechanism of THI against MCPs may foster the design of organic-based agents that modulate the biological activity of insect MCPs.

Acknowledgments

This work is financially supported by State Key Laboratory of the Discovery and Development of Novel Pesticide (No. 201101). This research is also supported by high-performance computing platform of Northwest A & F University.

Table S1
Binding free energy estimates for MCP–DF5 complexes.

Contribution	CPBHz–DF5		CPAHa–DF5		CPBh–DF5	
	Mean	Std	Mean	Std	Mean	Std
ΔE_{ele}	−76.21	6.49	−36.63	6.75	−82.70	5.42
ΔG_{vdW}	−16.98	4.45	−31.71	2.18	−23.34	3.86
ΔG_{np}	−2.98	0.15	−3.08	0.10	−3.59	0.19
ΔG_{PB}	66.57	5.49	64.96	5.65	84.64	7.29
ΔG_{cavity}	−2.98	0.15	−3.08	0.10	−3.59	0.19
ΔG_{gas}	−93.19	7.87	−68.34	7.10	−106.04	6.66
ΔG_{sol}	63.59	5.49	61.88	5.65	81.05	7.29
$-T\Delta S_{tot}$	724.81	10.20	826.86	10.48	837.39	8.65
ΔG_{bind}[a]	−29.60	4.79	−6.46	4.26	−25.00	4.81
ΔG_{bind}[b]	695.21	–	820.40	–	812.39	–

All values are given in kcal/mol.
[a] The predictions of binding energy do not include entropy effect.
[b] The predictions of binding energy include entropy effect.

Table S2
Binding free energy estimates for MCP–DF4 complexes.

Contribution	CPBHz–DF4		CPAHa–DF4		CPBh–DF4	
	Mean	Std	Mean	Std	Mean	Std
ΔE_{ele}	−12.24	3.63	−97.42	6.26	−56.90	4.68
ΔG_{vdW}	−29.38	2.49	−23.91	4.29	−47.50	2.88
ΔG_{np}	−3.23	0.34	−3.33	0.36	−4.04	0.21
ΔG_{PB}	24.95	4.31	72.79	4.11	91.08	5.46
ΔG_{cavity}	−3.23	0.34	−3.33	0.36	−4.04	0.21
ΔG_{gas}	−41.62	4.25	−121.33	4.68	−104.39	5.00
ΔG_{sol}	21.73	4.13	69.46	4.02	87.05	5.40
$-T\Delta S_{tot}$	18.62	4.30	24.02	5.56	25.34	7.57
ΔG_{bind}[a]	−19.89	3.36	−51.88	4.47	−17.34	4.59
ΔG_{bind}[b]	−1.27	–	−27.86	–	8.00	–

All values are given in kcal/mol.
[a] The predictions of binding energy do not include entropy effect.
[b] The predictions of binding energy include entropy effect.

Table S3
Binding free energy estimates for MCP–BSA complexes.

Contribution	CPBHz–BSA		CPAHa–BSA		CPBh–BSA	
	Mean	Std	Mean	Std	Mean	Std
ΔE_{ele}	−15.16	5.61	−7.91	2.40	−56.42	5.06
ΔG_{vdW}	−41.67	2.14	−37.90	2.02	−34.10	3.32
ΔG_{np}	−3. 75	0.13	−3.21	0.15	−3.34	0.16
ΔG_{PB}	59.58	7.24	38.72	4.62	67.53	5.38
ΔG_{cavity}	−3. 75	0.13	−3.21	0.15	−3.34	0.16
ΔG_{gas}	−56.83	5.88	−45.81	3.36	−90.52	4.63
ΔG_{sol}	55.83	7.20	35.50	4.55	64. 20	5.36
$-T\Delta S_{tot}$	21.90	9.02	19.14	7.03	17.75	6.55
ΔG_{bind}[a]	−1.00	6.82	−10.31	3.70	−26.32	4.22
ΔG_{bind}[b]	20.90	–	8.83	–	−8.57	–

All values are given in kcal/mol.
[a] The predictions of binding energy do not include entropy effect.
[b] The predictions of binding energy include entropy effect. ADDIN.

Appendix A. Supplementary material

Supplementary data related to this article can be found online at doi:10.1016/j.ibmb.2012.04.005.

References

Adler, M., Bryant, J., Buckman, B., Islam, I., Larsen, B., Finster, S., Kent, L., May, K., Mohan, R., Yuan, S., Whitlow, M., 2005. Crystal structures of potent thiol-based inhibitors bound to carboxypeptidase B. Biochemistry 44, 9339–9347.
Adler, M., Buckman, B., Bryant, J., Chang, Z., Chu, K., Emayan, K., Hrvatin, P., Islam, I., Morser, J., Sukovich, D., West, C., Yuan, S., Whitlow, M., 2008. Structures of potent selective peptide mimetics bound to carboxypeptidase B. Acta Cryst 64, 149–157.

Arolas, J.L., Lorenzo, J., Rovira, A., Castellà, J., Aviles, F.X., Sommerhoff, C.P., 2005. A carboxypeptidase inhibitor from the tick rhipicephalus bursa. J. Biol. Chem. 280, 3441–3448.

Bayés, A., Comellas-Bigler, M., Rodriguez de la Vega, M., Maskos, K., Bode, W., Aviles, F.X., Jongsma, M.A., Beekwilder, J., Vendrell, J., 2005. Structural basis of the resistance of an insect carboxypeptidase to plant protease inhibitors. Proc. Natl. Acad. Sci. USA 102, 16602–16607.

Bolter, C., Jongsma, M.A., 1997. The adaptation of insects to plant protease inhibitors. J. Insect Physiol. 43, 885–895.

Brito, L.O., Lopes, A.R., Parra, J.R., Terra, W.R., Silva-Filho, M.C., 2001. Adaptation of tobacco budworm Heliothis virescens to proteinase inhibitors may be mediated by the synthesis of new proteinases. Comp. Biochem. Physiol. B: Biochem. Mol. Biol. 128, 365–375.

Broadway, R.M., 1995. Are insects resistant to plant proteinase inhibitors? J. Insect Physiol. 41, 107–116.

Case, D.A., Darden, T.A., Cheatham, I., Simmerling, C.L., Wang, J., Duke, R.E., Luo, R., Crowley, M., Walker, R.C., Zhang, W., Merz, K.M., Wang, B., Hayik, S., Roitberg, A., Seabra, G., Kolossváry, I., Wong, K.F., Paesani, F., Vanicek, J., Wu, X., Brozell, S.R., Steinbrecher, T., Gohlke, H., Yang, L., Tan, C., Mongan, J., Hornak, V., Cui, G., Mathews, D.H., Seetin, M.G., Sagui, C., Babin, V., Kollman, P.A., 2008. AMBER 10. University of California, San Francisco, CA, USA.

Chang, C.A., Chen, W., Gilson, M.K., 2007. Ligand configurational entropy and protein binding. P. Natl. Acad. Sci. USA 104, 1534–1539.

David, W.C., William, N.L., 1989. Carboxypeptidase A. Acc. Chem. Res. 22, 62–69.

DeLano, W.L., 2010. The PyMolMolecular Graphics System. DeLano Scientific, Palo Alto, CA, USA.

Deng, N.J., Cieplak, P., 2009. Insights into affinity and specificity in the complexes of alpha-lytic protease and its inhibitor proteins: binding free energy from molecular dynamics simulation. Phys. Chem. Chem. Phys. 11, 4968–4981.

Essmann, U., Perera, L., Berkowitz, M., Darden, T.A., Lee, H., Pedersen, L., 1995. A smooth particle mesh Ewald method. J. Chem. Phys. 103, 8577–8593.

Estébanez-Perpiñá, E., Bayés, A., Vendrell, J., Jongsma, M.A., Bown, D.P., Gatehouse, J.A., Huber, R., Bode, W., Avilés, F.X., Reverter, D., 2001. Crystal structure of a novel mid-gut procarboxypeptidase from the cotton pest Helicoverpa armigera. J. Mol. Biol. 313, 629–638.

Fernández, D., 2009. Discovery and Characterization of Small Molecular Weight Metallocarboxypeptidase Inhibitors. Universitat Autònoma de Barcelona.

Fernández, D., Avilés, F.X., Vendrell, J., 2009a. Aromatic organic compounds as scaffolds for metallocarboxypeptidase inhibitor design. Chem. Biol. Drug des 73, 75–82.

Fernández, D., Avilés, F.X., Vendrell, J., 2009b. A new type of five-membered heterocyclic inhibitors of basic metallocarboxypeptidases. Eur. J. Med. Chem. 44, 3266–3271.

Fernández, D., Pallares, I., Vendrell, J., Avilés, F., 2010. Progress in metallocarboxypeptidases and their small molecular weight inhibitors. Biochimie 92, 1484–1500.

Gohlke, H., Kiel, C., Case, D.A., 2003. Insights into protein-protein binding by binding free energy calculation and free energy decomposition for the Ras–Raf and Ras–RalGDS complexes. J. Mol. Biol. 330, 891–913.

Gomis-Rüth, F.X., 2008. Structure and mechanism of metallocarboxypeptidases. Crit. Rev. Biochem. Mol. Biol. 43, 319–345.

Harsulkar, A.M., Giri, A.P., Patankar, A.G., Gupta, V.S., Sainani, M.N., Ranjekar, P.K., Deshpande, V.V., 1999. Successive use of non-host plant proteinase inhibitors required for effective inhibition of Helicoverpa armigera gut proteinases and larval growth. Plant Physiol. 121, 497–506.

Hass, G.M., Derr, J.E., Makus, D.J., Ryan, C.A., 1979. Purification and characterization of the carboxypeptidase isoinhibitors from potatoes. Plant Physiol. 64, 1022–1028.

Hu, G., Zhu, T., Zhang, S.L., Wang, D., Zhang, Q.G., 2010. Some insights into mechanism for binding and drug resistance of wild type and I50V V82A and I84V mutations in HIV-1 protease with GRL-98065 inhibitor from molecular dynamic simulations. Eur. J. Med. Chem. 45, 227–235.

Hummer, G., Rasaiah, J.C., Noworyta, J.P., 2001. Water conduction through the hydrophobic channel of a carbon nanotube. Nature 414, 188–190.

Jain, A.N., 2003. Surflex: fully automatic flexible molecular docking using a molecular similarity-based search Engine. J. Med. Chem. 46, 499–511.

Jakalian, A., Jack, D.B., Bayly, C.I., 2002. Fast, efficient generation of high-quality atomic charges. AM1-BCC model: II. parameterization and validation. J. Comput. Chem. 23, 1623–1641.

Jongsma, M.A., Baker, P.L., Peters, J., Bosch, D., Stiekema, W.J., 1995. Adaptation of spodoptera exigua larvae to plant proteinase inhibitors by induction of gut proteinase activity insensitive to inhibition. Proc. Natl. Acad. Sci. 92, 8041–8045.

Kollman, P.A., Massova, I., Reyes, C., Kuhn, B., Huo, S., Chong, L., Lee, M., Lee, T., Duan, Y., Wang, W., Donini, O., Cieplak, P., Srinivasan, J., Case, D.A., Cheatham, T.E.r., 2000. Calculating structures and free energies of complex molecules: combining molecular mechanics and continuum models. Acc. Chem. Res. 33, 889–897.

Kottalam, J., Case, D.A., 1990. Langevin modes of macromolecules: applications to crambin and DNA hexamers. Biopolymers 29, 1409–1421.

Lawrence, P.K., Koundal, K.R., 2002. Plant protease inhibitors in control of phytophagous insects. Electron. J. Biotechn 5, 93–109.

Lee, J., Kim, J.S., Seok, C., 2010. Cooperativity and specificity of cys2His2 zinc finger protein–DNA interactions: a molecular dynamics simulation study. J. Phys. Chem. B 114, 7662–7671.

Lee, T.S., Potts, S.J., Kantarjian, H., Cortes, J., Giles, F., Albitar, M., 2008. Molecular basis explanation for imatinib resistance of BCR-ABL due to T315I and P-loop mutations from molecular dynamics simulations. Cancer 112, 1744–1753.

Lin, F., Wang, R., 2010. Systematic Derivation of AMBER force field parameters Applicable to zinc-Containing systems. J. Chem. Theory Comput. 6, 1852–1870.

Migliolo, L., de Oliveira, A.S., Santos, E.A., Franco, O.L., de Sales, M.P., 2010. Structural and mechanistic insights into a novel non-competitive Kunitz trypsin inhibitor from Adenanthera pavonina L. seeds with double activity toward serine- and cysteine-proteinases. J. Mol. Graph. Model. 29, 148–156.

Obiol-Pardo, C., Rubio-Martinez, J., 2006. Comparative evaluation of MMPBSA and XSCORE to compute binding free energy in XIAP–peptide complexes. J. Chem. Inf. Model. 47, 134–142.

Oelschlaeger, P., Schmid, R.D., Pleiss, J., 2003. Modeling domino effects in enzymes: molecular basis of the substrate specificity of the bacterial metallo-β-lactamases IMP-1 and IMP-6. Biochemistry 42, 8945–8956.

Onufriev, A., Bashford, D., Case, D.A., 2000. Modification of the generalized born model suitable for macromolecules. J. Phys. Chem. B 104, 3712–3720.

Pang, Y.P., 1999. Novel zinc protein molecular dynamics simulations: steps towards antiangiogenesis for cancer treatment. J. Mol. Model. 5, 196–202.

Pang, Y.P., 2001. Successful molecular dynamics simulation of two zinc complexes bridged by a hydroxide in phosphotriesterase using the cationic dummy atom method. Proteins 45, 183–189.

Pang, Y.P., Xu, K., Yazal, J.E., Prendergast, F.G., 2000. Successful molecular dynamics simulation of the zinc-bound farnesyltransferase using the cationic dummy atom approach. Protein Sci. 9, 1857–1865.

Rees, D.C., Lipscomb, W.N., 1982. Refined crystal structure of the potato inhibitor complex of carboxypeptidase A at 2.5 Å resolution. J. Mol. Biol. 160, 475–498.

Ritchie, D.W., Kemp, G.J.L., 2000. Protein docking using spherical polar Fourier correlations. Proteins 39, 178–194.

Ryckaert, J., Ciccotti, G., Berendsen, H., 1977. Numerical integration of the cartesian equations of motion of a system with constraints: molecular dynamics of n-alkanes. J. Comput. Phys. 23, 327–341.

Vendrell, J., Querol, E., Avilés, F.X., 2000. Metallocarboxypeptidases and their protein inhibitors, structure, function and biomedical properties. Biochim. Biophys. Acta 1477, 284–298.

Wang, J., Wolf, R.M., Caldwell, J.W., Kollman, P.A., Case, D.A., 2004. Development and testing of a general amber force field. J. Comput. Chem. 25, 1157–1174.

Wang, X., Xu, X., Ma, Z., Huo, Y., Xiao, Z., Li, Y., Wang, Y., 2011. Dynamic mechanisms for pre-miRNA binding and export by Exportin-5. Rna 17, 1511–1528.

Wang, Y., Li, Y., Ma, Z., Yang, W., Ai, C., 2010. Mechanism of MicroRNA-target interaction: molecular dynamics simulations and thermodynamics analysis. PLoS Comput. Biol. 6, e1000866.

Wu, Y., Llewellyn, D., Mathews, A., Dennis, E.S., 1997. Adaptation of Helicoverpa armigera (Lepidoptera: Noctuidae) to a proteinase inhibitor expressed in transgenic tobacco. Mol. Breeding 3, 371–380.

Xu, X., Yang, W., Wang, X., Li, Y., Wang, Y., Ai, C., 2011. Dynamic communication between androgen and coactivator: mutually induced conformational perturbations in androgen receptor ligand-binding domain. Proteins 79, 1154–1171.

Zoete, V., Michielin, O., 2007. Comparison between computational alanine scanning and per-residue binding free energy decomposition for protein–protein association using MM-GBSA: application to the TCR-p-MHC complex. Proteins 67, 1026–1047.